Hollow Block Copolymer Nanoparticles through a Spontaneous One-step Structural Reorganization

Nikos Petzetakis,[†,‡] Mathew P. Robin,[†,‡] Joseph P. Patterson,[†] Elizabeth G. Kelley,[§] Pepa Cotanda,[†] Paul H. H. Bomans,[⊥] Nico A. J. M. Sommerdijk,[⊥] Andrew P. Dove,[†] Thomas H. Epps, III,[§,*] and Rachel K. O'Reilly[†,*]

[†]Department of Chemistry, Library Road, University of Warwick, Coventry, CV4 7AL, U.K., [§]Department of Chemical and Biomolecular Engineering, University of Delaware, Newark, Delaware 19716, United States, and [⊥]Laboratory of Materials and Interface Chemistry and Soft Matter CryoTEM Research Unit, Department of Chemical Engineering and Chemistry, Eindhoven University of Technology, P.O. Box 513, 5600 MB Eindhoven, The Netherlands. [‡]These authors contributed equally to this work.

ABSTRACT The spontaneous one-step synthesis of hollow nanocages and nanotubes from spherical and cylindrical micelles based on poly(acrylic acid)-*b*-polylactide (P(AA)-*b*-P(LA)) block copolymers (BCPs) has been achieved. This structural reorganization, which occurs simply upon drying of the samples, was elucidated by transmission electron microscopy (TEM) and atomic force microscopy (AFM). We show that it was necessary to use stain-free imaging to examine these nanoscale assemblies, as the hollow nature of the particles was obscured by application of a heavy metal stain. Additionally, the internal topology of the P(AA)-*b*-P(LA) particles could be tuned by manipulating the drying conditions to give solid or compartmentalized structures. Upon resuspension, these reorganized nanoparticles retain their hollow structure and display significantly enhanced loading of a hydrophobic dye compared to the original solid cylinders.

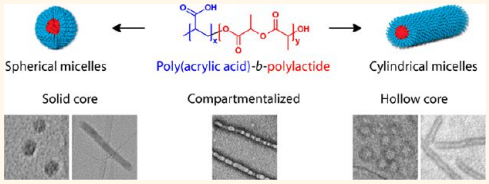

KEYWORDS: polymer · hollow nanostructures · drying · microscopy · solution assembly · block copolymer · nanoparticles

Hollow nanoparticles of either spherical or cylindrical morphologies (nanocages and nanotubes) are highly desirable due to their potential utility as nanoreactors,[1] nanocontainers,[2] purification agents,[3] delivery vehicles,[4] and nanofluidic materials.[5] Several synthetic approaches have been developed for their fabrication in solution and in bulk, including layer-by-layer deposition,[6] templated synthesis,[7] and block copolymer (BCP) self-assembly.[8,9] The latter is of particular importance due to the versatility of BCPs for generating nanoparticles of controlled size and shape (spheres,[10,11] cylinders,[12,13] and bilayers).[14,15]

Pioneering work by Wooley et al. utilized poly(acrylic acid)-*b*-polyisoprene (P(AA)-*b*-PI) spherical micelles as scaffolds for the synthesis of nanocages by sequential shell cross-linking and core degradation,[8] an approach that was subsequently extended to other BCP systems.[16−18] Liu and co-workers applied a similar methodology to spherical and cylindrical reverse micelles to fabricate nanocages and nanotubes in organic solvents.[19,20] Recently, Ho et al. utilized the bulk phase separation of polystyrene-*b*-polylactide (PS-*b*-P(LA)) block copolymers to form hexagonally ordered cylinders, with subsequent P(LA) hydrolysis affording PS nanotubes.[21] Cohen and co-workers reported the formation of cavitated spherical nanoparticles based on polymeric micelle templates by a core-swelling/shell-rupture method performed on micelle thin films.[22] While these reports illustrate the potential of BCP self-assembly for the synthesis of hollow nanoparticles, they all involve additional synthetic and characterization steps. Efficient, reliable, and scalable processing methods for hollow nanoparticle generation are still needed to match the experimental simplicity of BCP self-assembly.

Two common real-space approaches for examining BCP self-assembled nanostructures are conventional transmission electron microscopy (TEM) and cryogenic-TEM (cryo-TEM). In many conventional TEM experiments, samples are imaged in the presence of heavy metal staining agents that are essential for enhancing the otherwise poor electron density contrast between copolymer domains, and between the polymer nanostructures and the support.[23] We note

* Address correspondence to thepps@udel.edu, R.K.O'Reilly@warwick.ac.uk.

Received for review September 6, 2012 and accepted January 31, 2013.

Published online February 07, 2013
10.1021/nn400272p

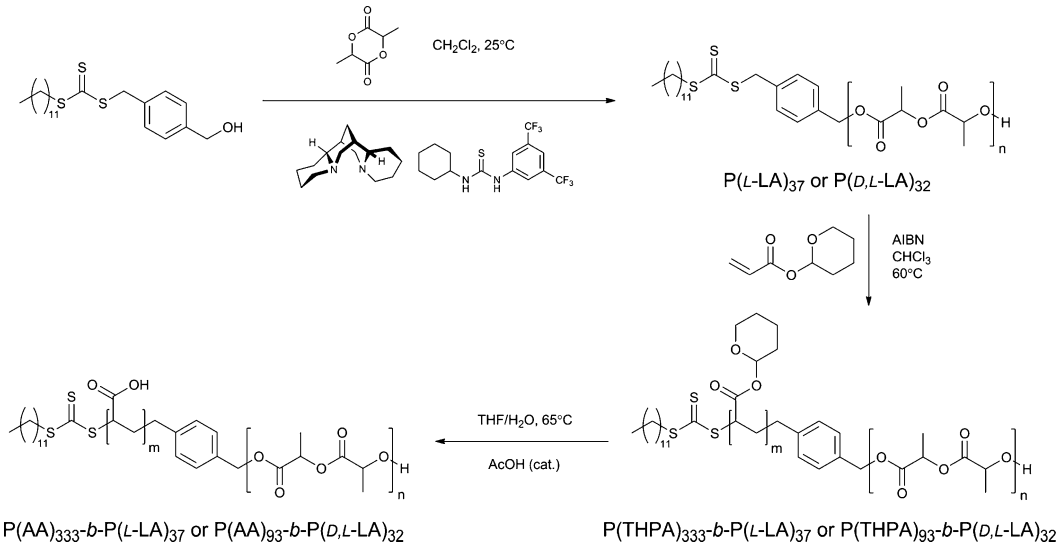

Scheme 1. Synthesis of P(AA)-*b*-P(LA) Amphiphilic Block Copolymers

that there are cases where low voltage TEM[24] and energy filtered-TEM (EF-TEM),[25,26] for example, also can be used to overcome these contrast limitations. Though there have been a small number of studies on the effects of drying and staining procedures on the examination of BCP solution assemblies,[27,28] these effects have not been explored in systematic detail. This has not only led to misinterpretation of some TEM-based analyses of solution-based assemblies,[29] but it also presents a significant barrier to the discovery of new phenomena that spontaneously occur upon the drying of nanostructured polymer specimens.

Recently, it has been demonstrated that dry state TEM can be performed using a graphene oxide (GO) support.[30,31] The GO substrate allows organic polymer-based particles (low−z materials) to be imaged without heavy metal stains. Thus, all the structural information of the dried particles is retained and directly imaged. Herein, we demonstrate the spontaneous formation of hollow block copolymer nanoparticles examined through this sample preparation technique. Hollow spherical (nanocages) and open-ended cylindrical (nanotubes) particles are produced by simply drop-casting aqueous solutions of P(AA)-*b*-P(LA) micelles onto GO substrates. The extent of this spontaneous structural reconstruction is tunable, as shown below. By altering the method of dehydration during the casting and drying process, core-compartmentalized or solid core−shell nanoparticles were produced in a controlled fashion. These hollow nanoparticles can be "harvested" from a surface by resuspension, and they have been demonstrated to display increased uptake of small molecule hydrophobic cargoes compared to the precursor cylindrical micelles.

RESULTS AND DISCUSSION

Cylindrical and Spherical Micelle Synthesis. Both cylindrical and spherical polymeric micelle solutions were obtained from poly(acrylic acid)-*b*-polylactide (P(AA)-*b*-P(LA)) block copolymers, where poly(tetrahydropyran acrylate) [P(THPA)] was used as a precursor to P(AA), as reported previously (Scheme 1)[32] (see Supporting Information for further polymer synthesis and characterization details). Incorporation of a semicrystalline L-lactide block (P(L-LA)) followed by crystallization-driven self-assembly afforded $P(AA)_{333}$-*b*-$P(L\text{-}LA)_{37}$ cylindrical micelles of controllable length.[13] Alternatively, the use of an amorphous D,L-lactide block (P(D,L-LA)) with subsequent P(THPA) hydrolysis and self-assembly of the resultant amphiphile produced $P(AA)_{93}$-*b*-$P(D,L\text{-}LA)_{32}$ spherical micelles.

Solution-state characterization confirmed the expected core−shell structure of these cylindrical and spherical micelles. Cryo-TEM also gave valuable information regarding the morphological identity of the nanoparticles in their solution state. This information was particularly useful for the cylinders, whose light and neutron scattering data analysis was more challenging due to the particle length scales and anisotropy. Analysis of the cryo-TEM data for the cylindrical micelles confirmed the presence of a solid core, with no distinct corona contrast noted (Figure 1a). The lack of corona contrast is attributed to solvation of the PAA chains; a common feature in acrylic acid based assemblies. From the cryo-TEM images, the average core radius of the cylindrical micelles was 16.0 ± 1.5 nm. To further characterize the nanoscale structure of the cylinders, small angle neutron scattering (SANS) experiments were performed on samples prepared in D_2O (see Methods section for further details regarding sample preparation). The SANS data and pair distance distribution function [P(*r*)] for $P(AA)_{333}$-$P(L\text{-}LA)_{37}$ are shown in Figure 1b.[33,34] The tail at larger *r* in the P(*r*) supports that the micelles are elongated, with a radial cross-section of 27 ± 2 nm.[34−36] Comparing the overall

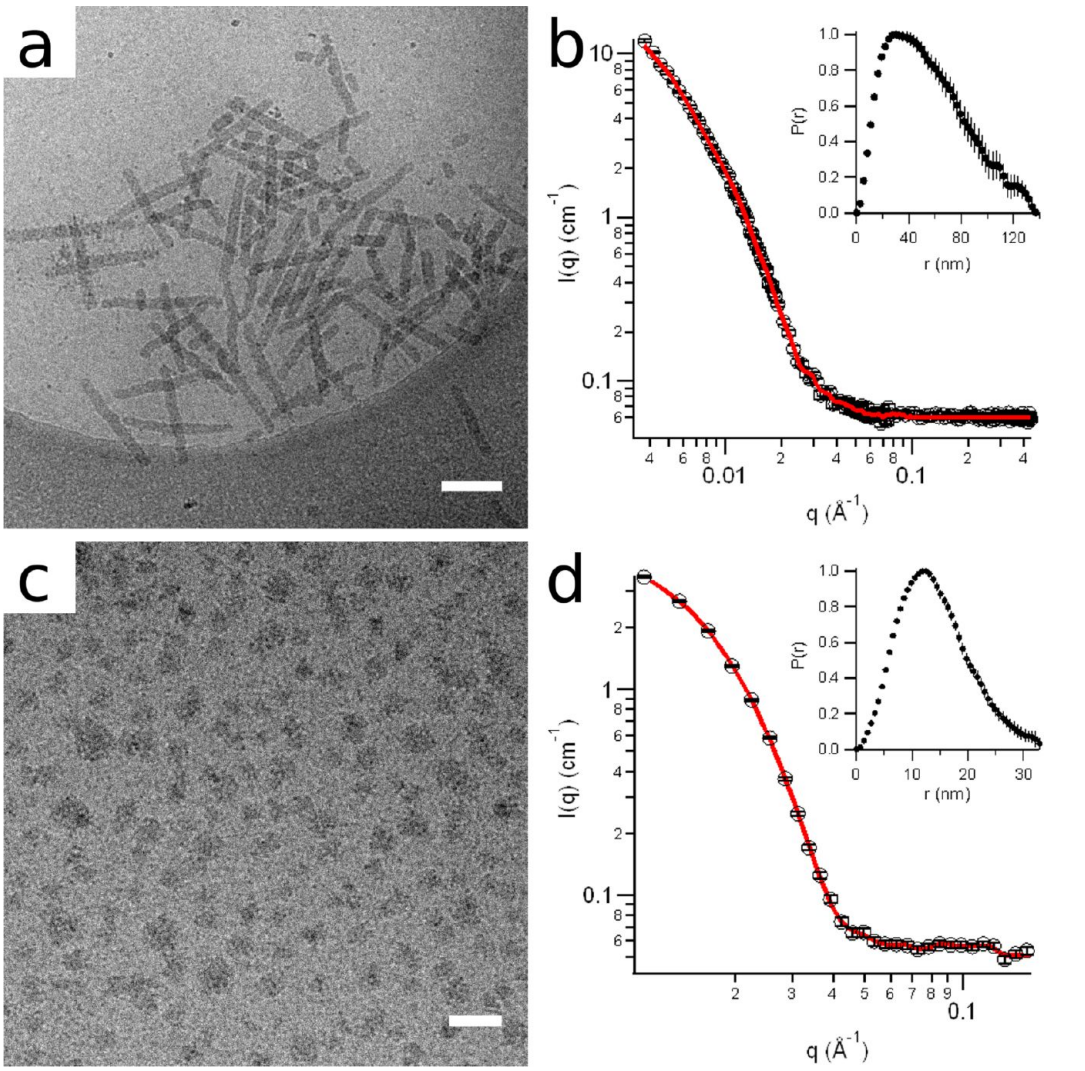

Figure 1. Cryo-TEM image of (a) $P(AA)_{333}$-*b*-$P(L\text{-}LA)_{37}$ cylindrical micelles (scale bar = 200 nm) and (c) $P(AA)_{93}$-*b*-$P(D,L\text{-}LA)_{32}$ spherical micelles (scale bar = 50 nm); SANS data (symbols) and fit by the indirect Fourier transformation (line) for (b) $P(AA)_{333}$-*b*-$P(L\text{-}LA)_{37}$ cylindrical micelles in D_2O; inset: pair distance distribution function [P(*r*)] and d) $P(AA)_{93}$-*b*-$P(D,L\text{-}LA)_{32}$ spherical micelles.

radial cross-section from SANS (27 ± 2 nm) to the core radius from cryo-TEM (16.0 ± 1.5 nm), indicates the presence of a core−shell structure with a PAA corona thickness of ~11 nm. Further analysis of the SANS data with a form factor model for cylinders[37] suggested that the cylinders were greater than 100 nm in length; however, the fit results were not sensitive to values larger than 100 nm.

For the spherical micelles, cryo-TEM indicates the presence of a solid core with average core radius of 8.9 ± 0.6 nm (Figure 1c). Comparing the core size and the number average hydrodynamic radius (R_h) of 13.6 nm (Figure S4, Supporting Information) from dynamic light scattering (DLS), gave a PAA corona thickness of 4.7 nm, suggestive of crew-cut micelles. Analysis of the P(*r*) from the SANS data (Figure 1d) further supports that the spherical micelles were solid (*i.e.*, not hollow) in solution,[34] giving a radius of gyration (R_g) of 11 nm. Additionally, the obtained R_g/R_h ratio of 0.81 is consistent with the theoretical value for hard spheres (0.78).[38,39]

Hollow nanoparticle synthesis. Aqueous solutions of cylindrical and spherical micelles (0.25 g·L^{-1}) were drop cast onto GO TEM grids and imaged directly. First, a drop of GO dispersed in nanopure water was deposited on a lacey carbon support to give a virtually electron transparent substrate. Then 2 μL of micelle solution was slowly air-dried to the grid in a desiccator, with full evaporation of the solvent taking 30 min.[31] The resulting images showed that both the cylindrical and spherical micelles had undergone a spontaneous cavitation on drying on the grid (Figures 2a and 3a). These hollow cylinders were noted uniformly across the GO TEM grids and were found to have an average core radius (R_{core}) of 9.8 ± 0.9 nm. Additionally, the cylinders had lower electron density at the two ends, strongly suggesting the formation of nanotubes. This formation of nanotubes is related to the crystallization driven

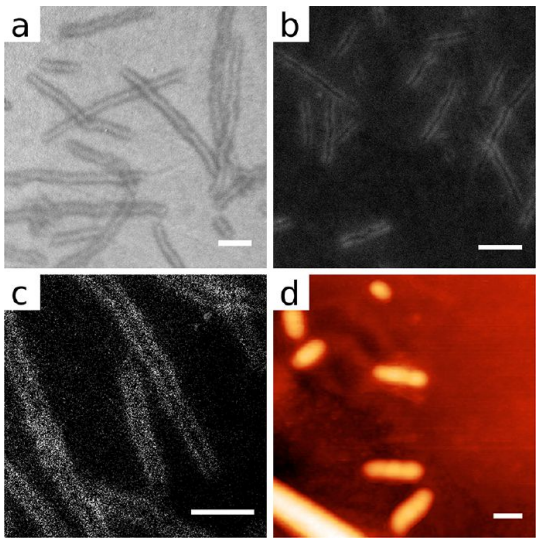

Figure 2. (a) TEM image of hollow $P(AA)_{333}$-*b*-$P(L\text{-}LA)_{37}$ cylinders; (b) HAADF-STEM image of hollow $P(AA)_{333}$-*b*-$P(L\text{-}LA)_{37}$ cylinders; (c) EF-TEM carbon map of hollow $P(AA)_{333}$-*b*-$P(L\text{-}LA)_{37}$ cylinders; (d) AFM image of hollow $P(AA)_{333}$-*b*-$P(L\text{-}LA)_{37}$ cylinders. All scale bars = 100 nm.

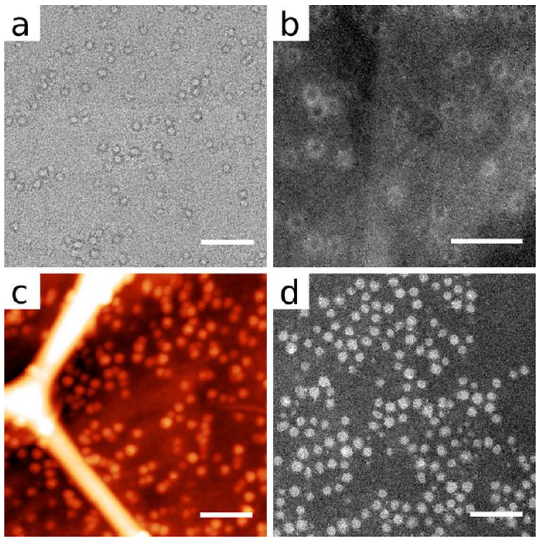

Figure 3. (a) TEM image of hollow $P(AA)_{93}$-*b*-$P(D,L\text{-}LA)_{32}$ spheres (scale bar = 100 nm); (b) EF-TEM carbon map of hollow $P(AA)_{93}$-*b*-$P(D,L\text{-}LA)_{32}$ spheres (scale bar = 100 nm); (c) AFM image of hollow $P(AA)_{93}$-*b*-$P(D,L\text{-}LA)_{32}$ spheres (scale bar = 200 nm); (d) PTA stained TEM image of hollow $P(AA)_{93}$-*b*-$P(D,L\text{-}LA)_{32}$ spheres (scale bar = 100 nm).

self-assembly methodology that was used, which is known to produce cylinders containing uncapped ends.[40]

To further examine the particles and confirm that the noted electron density contrast was not the result of phase contrast; the same GO grids also were characterized by high angle annular dark field scanning TEM (HAADF-STEM). In this method, the collected electrons are scattered in wide angles where incoherent scattering dominates, and therefore exclusively z-contrast dependent images are created. Again, the particles appeared hollow, and the contrast effects were similar to conventional TEM, likely ruling out phase contrast as a source of this observed effect (Figure 2b). Further analysis by energy-filtered TEM (EF-TEM) also supported that the noted core–shell contrast was a consequence of a decreased density of carbon and oxygen (and therefore polymer) at the center of the cylinders (Figure 2c) and spheres (Figure 3b), revealing that the micelles had dried to form truly hollow structures on the GO surface. One of the previously demonstrated advantages of GO-coated grids is the ability to use them for multi-technique imaging of the same sample grid.[31] Atomic force microscopy (AFM) analysis of the hollow particles dried to a GO grid revealed that the cylindrical nanoparticles had not collapsed, but rather had retained their circular cross-section (Figure S9 and S10, Supporting Information). Additionally, the AFM height measurements (32.0 ± 2.1 nm) were in reasonable agreement with the cylindrical micelle diameter values obtained by TEM (28.0 ± 1.8 nm), which indicates that the structures could be described as nanotubes consisting of 1-dimensional nanochannels with an internal diameter of 20 nm and a wall thickness of ~6 nm (Figure 2d). Traditional dry-state TEM using the negative stain phosphotungstic acid (PTA) revealed cylindrical nanoparticles with $D_{micelle}$ = ~27 nm (Figure S13, Supporting Information) in reasonable agreement with unstained images. However the staining process obscured the hollow nature of the particles, with a uniform electron density found across all nanoparticles.

Analysis of the spherical micelles cast on the GO surfaces also showed a drying effect with a greater density at their edges than at their centers. These hollow spheres were found to have an average radius (R_{av}) of 9.1 ± 1.1 nm (Figure 3a). In addition, AFM analysis indicated that the hollow spheres had an average height of 6.6 ± 1.8 nm above the surface (Figure 3c, S11 and S12, Supporting Information), which suggests that the particles had collapsed to some extent, as this height is significantly less than the particle diameter. Again, dry-state TEM using PTA stain revealed spherical particles with sizes in agreement with unstained images, R_{av} = 8.9 ± 1.3 nm (Figure 3d).

The extent of the structural reconstruction of the nanoparticles can be controlled by altering the drying method. In contrast to the slow evaporation method (Figure 2a), drop-casting of the cylindrical micelles on a GO grid followed by blotting after 1 min (fast-drying) produced dried particles that had undergone a reconstruction to form necklace-like structures (Figure 4a and S15, Supporting Information). In this case, the compartments have an average length of 23.0 ± 3.1 nm and are separated by P(LA) layers that are as thin as 4 nm. This effect is related to the nonuniform degree of crystallinity along the core of the cylinders. We hypothesize that the blotting/fast-drying method provides less time for morphological rearrangement.

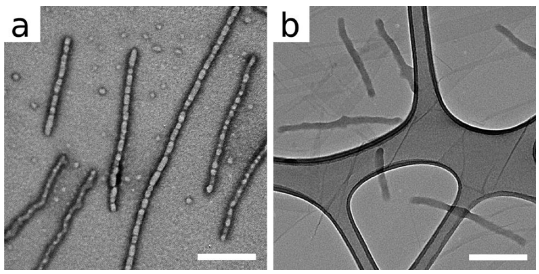

Figure 4. TEM images of $P(AA)_{333}$-*b*-$P(L\text{-}LA)_{37}$ cylindrical micelles on GO substrates prepared by (a) blotting and (b) freeze-drying. All scale bars = 200 nm.

As a consequence, the "hollowing" of the cylinders does not occur uniformly along the cylinder core, likely resulting from the fact that the crystalline P(LA) regions are relatively stable in comparison to the amorphous material. Furthermore, structural reconstructions can be eliminated entirely by using a freeze-drying preparation method for both cylinders (Figure 4b and S16, Supporting Information) and spheres (Figure S18, Supporting Information). After drop-casting the sample, the GO grid was immediately plunged into liquid nitrogen and freeze-dried to remove water.[41] The resulting TEM images of both spherical and cylindrical micelles revealed solid particles with a uniform density across their diameter, in agreement with their solution-state nanostructures, as determined by cryo-TEM.

"Harvesting" of Hollow Nanoparticles. After their structural reorganization upon drying, hollow nanotubes could be "harvested" by resuspension in water. This was achieved by the addition of a solution of solid micelles (1 mL, 0.25 $g \cdot L^{-1}$) to a 1.5 mL Eppendorf tube, that was subsequently placed in a desiccator at reduced pressure to slowly remove the water. After 16 h, the particles had dried to the plastic surface of the Eppendorf tube, at which point addition of nanopure water allowed resuspension of the hollow particles at a chosen concentration.

Resuspended nanotubes were visualized by cryo-TEM (Figure 5). There is a clear contrast difference across the diameter of the hollow nanotubes, revealing a lower density (*i.e.*, hollow) core, in comparison to the solid walls. The average radius of the hollow core is 8.0 $\pm$ 1.3 nm, with the higher contrast polylactide adding a further 13.8 nm to radius (giving a total of 21.8 $\pm$ 2.4 nm for the visible radius of the particles). This lower density core indicates that the hollow nanotubes likely have an internal water pool, suggesting that the hydrophilic poly(acrylic acid) forms both the internal and external interfaces. Comparison with the solid micelles (Figure 1), which have a uniform contrast across their diameter, gives clear evidence that the hollow nanotubes have survived the resuspension process. Also, it was found that the hollow nanotubes are open-ended, in agreement with the hollow structures imaged on a GO support (Figure 2). As expected,

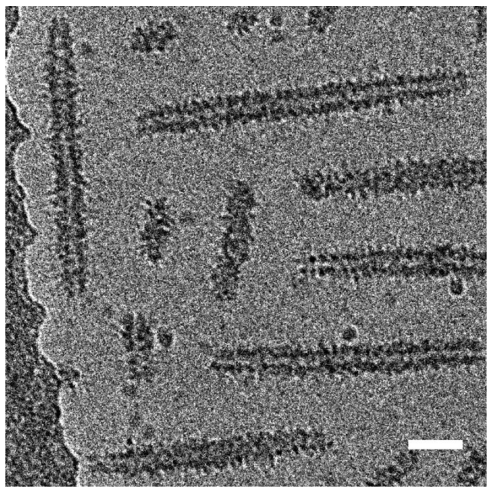

Figure 5. Cryo-TEM image of "harvested" hollow cylindrical nanotubes. Scale bar = 100 nm.

when a solution of solid micelles was freeze-dried and then resuspended, the cryo-TEM images showed unchanged solid particles.

When the "harvesting" procedure was repeated for the hollow spherical nanocages, cryo-TEM images again provided evidence that the resuspended particles had undergone a morphology change (Figure S19, Supporting Information). However, due to the much smaller size of the spherical particles in comparison to the cylinders, it was difficult to unambiguously identify spheres with a hollow core.

The solution of hollow cylinders shown in Figure 5 was reimaged by cryo-TEM one month after resuspension (Figure S20, Supporting Information). On this occasion only a small proportion of the cylinders retained a hollow core, while the majority had re-equilibrated to their initial solid core structure.

Mechanism of Hollow Particle Formation. We propose that the spontaneous cavitation of the P(AA)-*b*-P(LA) nanoparticles when slowly dried to a substrate is due to hydrogen-bonding between the polylactide core and poly(acrylic acid) corona, which will become fully protonated upon drying. During the slow evaporation preparation method, a contraction of the core to the corona occurs, leaving a hollow center (Figure 6). When the hollow particles are resuspended in water, it is expected that the hydrogen-bonding between the poly(lactide) and the now solvated poly(acrylic acid) blocks would be disrupted, leading to aggregation of poly(lactide) chains. As the block ratio P(AA):P(LA) > 1, it is also possible that some poly(acrylic acid) units remain hydrogen bonded to poly(lactide), while the remainder are solvated. As discussed above, it was observed that this kinetically trapped hollow state re-equilibrated over time to the initial solution state morphology. We believe that this proposed collapsed structure for the hollow particles is more likely than a bilayer structure for a number of reasons. The high

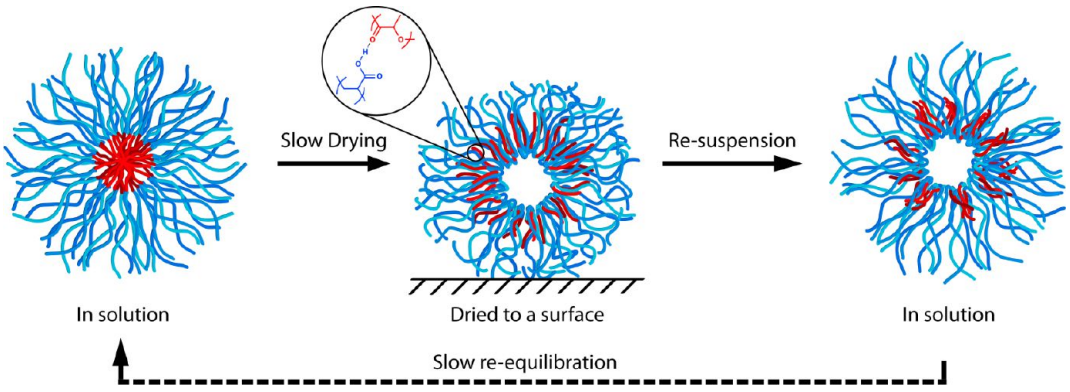

Figure 6. Schematic depiction of hollow particle formation, showing a cross-section of a cylindrical or spherical particle.

curvature of the initial micelles resulting from the large P(AA):P(LA) block ratio, the similarity in size of particles before and after hollowing, and the large energetic barrier required for the significant reorganization to a bilayer structure all disfavor the existence of a bilayer.

In order to test this theory, poly(ethylene oxide) [P(EO)] was utilized as an alternative, non hydrogen-bond donor corona block. Solid spherical micelles with number average R_h of 8.0 nm (as measured by DLS) were obtained from commercially available $P(EO)_{5k}$-*b*-$P(_{D,L}\text{-LA})_{4k}$ as previously demonstrated.[42,43] Then, these particles were dried on GO TEM grids using the same slow evaporation preparation used with the P(AA)-*b*-P(LA). The resulting nonstained TEM images revealed a uniform electron density across the surface of the particles, with the complete absence of hollow structures, indicating that no structural reconstruction had occurred (Figure S21, Supporting Information).

We anticipate that other particles containing different hydrogen bonding donor–acceptor polymer blocks (potentially already existing on the shelves of many laboratories) will be able to undergo similar spontaneous reconstructions, providing direct access to nanocages and nanotubes of different chemical compositions and functionalities. Furthermore, it is conceivable that one could control the internal tube/cage diameter simply by tuning the length of the core block of the BCP.

Hollow Particle Loading. The hydrophobic dye Nile Red has previously been used as model small molecule cargo to demonstrate the increased loading capacity of nanocages, when compared to analogous solid nanoparticles.[1] To investigate whether previously "harvested" solution of hollow P(AA)-*b*-P(LA) particles had an increased encapsulation ability compared to their solid precursors, a series of Nile Red loading experiments was performed. First, aqueous solutions (1 mL, 0.25 $g \cdot L^{-1}$) of solid cylindrical and spherical micelles, and a control (1 mL nanopure water) were added to Nile Red (2 mg), and the mixtures were incubated for

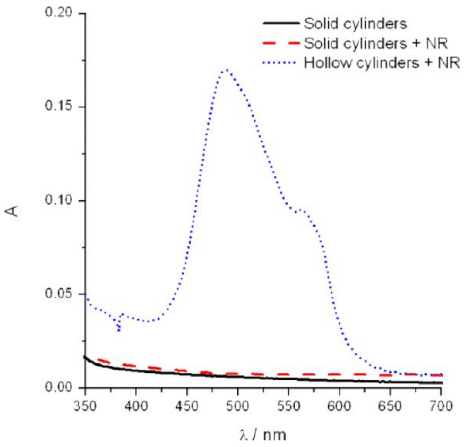

Figure 7. UV–vis spectra for Nile Red (NR) loading experiments with cylindrical nanoparticles.

16 h. After filtration (0.45 μm Nylon filter) and dialysis to remove excess Nile Red, UV–vis spectroscopy revealed a minor increase in absorption compared to the control sample. However, when the procedure was repeated with the resuspended hollow nanotubes (see Figure 5), a significant absorption due to Nile Red was observed, which indicates the sequestration of dye by the hollow nanotubes (Figure 7). Interestingly, when the procedure was repeated with hollow nanocages, there was no improvement in uptake of Nile Red, compared to the original solid spherical micelles (Figure S22, Supporting Information). It is proposed that the open ends of the hollow cylinders allow diffusion of Nile Red into the vacant core, leading to a greater loading ability in comparison to the solid cylinders. We propose that the lack of such an opening in the spheres provides a similar energetic barrier for crossing the poly(acrylic acid) corona for both solid and hollow particles, thus no improvement in loading is noted for the hollow nanocages.

CONCLUSIONS

In summary, we have demonstrated that cylindrical and spherical block copolymer nanoparticles of P(AA)-*b*-P(LA) undergo a spontaneous cavitation upon drying

on a substrate to form nanocages and nanotubes of controlled length. We have shown that by manipulating the drying conditions, we can impart control over the morphology of the nanostructures formed. Additionally, hollow particles can be "harvested" by the resuspension of slowly dried micelles, and these hollow nanotubes show an increased loading capacity for a model hydrophobic dye. Furthermore, it was illustrated that this phenomenon is obscured when applying heavy metal staining agents commonly used in transmission electron microscopy. The spontaneous structural reconstruction method presented herein should have wide-ranging potential for the synthesis of a broad range of hollow particles.

METHODS

Micelle Self-assembly. Spherical micelles were formed by direct dissolution of the lyophilized polymer. $P(AA)_{93}$-*b*-$P(_{D,L}$-$LA)_{32}$ was added to nanopure water to a final polymer concentration of 0.25 $g \cdot L^{-1}$. The solution was stirred at 55 °C for 3 h before being stirred at room temperature overnight. Cylindrical micelles of $P(AA)_{333}$-*b*-$P(_{L}$-$LA)_{37}$ were formed by crystallization driven self-assembly, which takes place *in situ* sequentially after the PTHPA block hydrolysis of $P(THPA)_{333}$-*b*-$P(_{L}$-$LA)_{37}$. The cylindrical micelles were redispersed in nanopure water by direct dissolution at 0.25 $g \cdot L^{-1}$. By altering the tetrahydrofuran (THF) content during the hydrolysis process cylinders of predictable lengths can be generated.

Formation of Hollow P(AA)-*b*-P(LA) Nanocages and Nanotubes by Slow Evaporation. Solutions of micellar assemblies (2 μL) were drop-cast onto a preprepared GO TEM grid. Then, the grid was left to air-dry for 30 min in a desiccator. The dried grid could be directly imaged by TEM, AFM, or SEM. Alternatively, phosphotungstic acid (PTA) stain (2 μL) was applied to the sample on the grid and blotted after 1 min to give stained grids for additional TEM analysis.

Formation of Compartmentalized Necklace like $P(AA)_{333}$-*b*-$P(_{L}$-$LA)_{37}$ Cylindrical Nanoparticles by Blotting. Solutions of $P(AA)_{333}$-*b*-$P(_{L}$-$LA)_{37}$ cylindrical micelles (2 μL) were drop-cast onto a preprepared GO TEM grid. Then, the grid was left to air-dry for 1 min before excess solution was removed by blotting. The dried grid could be directly imaged by TEM, AFM, or SEM.

Formation of Solid P(AA)-*b*-P(LA) Spherical and Cylindrical Nanoparticles by Freeze-drying. Solutions of micellar assemblies (2 μL) were drop-cast onto a preprepared GO TEM grid. Then, the grid was immediately plunged into liquid nitrogen, and water was removed by freeze-drying the grid inside a glass ampule. The dried grid could be directly imaged by TEM, AFM, or SEM.

"Harvesting" of Hollow P(AA)-*b*-P(LA) Spherical and Cylindrical Nanoparticles. Solutions of micellar assemblies (1 mL, 0.25 mg) were added to a 1.5 mL Eppendorf tube. The tube was placed in a desiccator (P_2O_5), at reduced pressure (10 mbar) for 16 h. Addition of a known quantity of nanopure water produced solutions of hollow nanoparticles at the desired concentration.

Nile Red Loading. A solution of nanoparticles (1 mL, 0.25 $g \cdot L^{-1}$) was added to an excess of Nile Red (2 mg). The mixture was stirred for 16 h, before filtration (0.45 μm Nylon syringe filter) and dialysis (Millipore "Amicon Ultra" centrifugal filter 10 kDa) to remove excess Nile Red. A control experiment using Nile Red (2 mg) and nanopure water (1 mL) was used as a background for UV–vis spectrometry. Spectra were normalized using the absorption of the polymeric RAFT end-group (λ_{max} = 307 nm).

Self-assembly of $P(EO)_{5k}$-*b*-$P(_{D,L}$-$LA)_{4k}$ to Give Spherical Micelles, and Subsequent Formation of Solid Nanoparticles. $P(EO)_{5k}$-*b*-$P(_{D,L}$-$LA)_{4k}$ (10 mg) was dissolved in THF (5 mL) by sonicating for 2 h. Nanopure water (5 mL) was added dropwise to the polymer solution using a metering pump, and the mixture was stirred overnight at room temperature. Then, the mixture was exhaustively dialyzed (MWCO 3.5 kDa dialysis tubing) against nanopure water. The resulting solution was drop-cast onto a preprepared GO TEM grid. The grid was left to air-dry for 30 min in a desiccator. The dried grid could be directly imaged by TEM, AFM, or SEM.

Transmission Electron Microscopy (TEM). Dry-stained images were obtained on 300 mesh Formvar/carbon grids. GO imaging was performed on 400 mesh lacy carbon films that contain deposited GO films. GO solutions[30] (0.10–0.15 $g \cdot L^{-1}$) were sonicated for 30 s prior to use. Lacey carbon grids (400 Mesh, Cu) (Agar Scientific) were cleaned using air plasma from a glow-discharge system (2 min, 20 mA). This step is not essential, but increases the hydrophilicity of the lacy carbon, which improves the coverage of GO to typically >70%. One drop (~0.08 mL) of the sonicated GO solution was deposited onto each grid and left to air-dry for 30 min. Once dry, the grids could be stored for several weeks before sample deposition. A video abstract is also available on how to prepare the GO grids.[44] Average sizes of the micelles were determined from counting the sizes of at least 100 particles for 3 different images. Images were taken using a Jeol 2010F TEM operated at 200 kV and imaged using a GatanUltrascan 4000 camera. Images were captured using Digital Micrograph software (Gatan).

The cryo-TEM image in Figure 5 was taken a Jeol 2010F TEM operated at 200 kV and imaged using a GatanUltrascan 4000 camera. Images were captured using Digital Micrograph software (Gatan). A 3 μL droplet the sample solution at 25 °C was added to a holey carbon-coated copper grid, and the grid was blotted to remove excess solution. Subsequently, the grid was plunged into liquid ethane to vitrify the sample. The temperature of the cryo-stage was maintained below −170 °C. All other cryo-TEM images were taken at the Laboratory of Materials and Interface Chemistry of Eindhoven University of Technology. Sample preparation for cryo-TEM was carried out in an automated vitrification robot (FEI Vitrobot Mark III) using liquid ethane as cryogen. TEM grids (Quantifoil R2/2, Quantifoil Micro Tools GmbH, Jena, Germany) were glow discharged prior to use in a Cressington 208 carbon coater for 40 s. CryoTEM samples were imaged with the TU/e CryoTitan (FEI,www.cryotem.nl). The CryoTitan is equipped with a field emission gun (FEG), a post column Gatan Energy Filter (GIF) and was operated at 300 kV. Images were recorded on a post-GIF 2k x 2k Gatan CCD camera using zero-loss energy filtering with a 20 eV energy window.

Atomic Force Microscopy (AFM) and Scanning Electron Microscopy (SEM). AFM was conducted in tapping mode on a Multimode AFM with Nanoscope IIIA controller with Quadrex, or an Asylum Research MFP3D-SA. Silicon AFM tips (MikroMasch NSC18) were used with a nominal spring constant and resonance frequency of 3.5 N/m and 75 kHz, respectively. SEM images were acquired on a Zeiss Supra55VP operating at an accelerating voltage of 2 kV.

Small Angle Neutron Scattering (SANS). SANS data for $P(AA)_{93}$-*b*-$P(_{D,L}$-$LA)_{32}$ were collected at the ISIS neutron facility, Rutherford Appleton Laboratories, on the time-of-flight LOQ diffractometer. The incident wavelength range of 2.2–10 Å gave rise to a q-range of 0.009–0.249 $Å^{-1}$. Absolute intensities for I(Q) (cm^{-1}) were determined within 5% by measuring the scattering from a partially deuterated polymer standard. Standard procedures for data treatment were employed.[45] Measurements were made at 25 °C, and the sample was prepared in D_2O and run in a 2 mm quartz cell.

SANS data for $P(AA)_{333}$-*b*-$P(_{L}$-$LA)_{37}$ in D_2O were collected at the National Institute of Standards and Technology (NIST) Center for Neutron Research (NCNR). Experiments were performed on the NG-7 30 m SANS instrument using an incident wavelength of 6.0 Å with a wavelength spread ($\Delta\lambda/\lambda$) of 0.12 and sample to detector distances of 1.0, 4.0, and 13.5 m to cover a scattering vector range from 0.004 $Å^{-1} < q < 0.4$ $Å^{-1}$. Absolute intensities were determined using the direct beam flux method and the data were reduced using standard procedures provided by NIST.[37]

The pair distance distribution function [P(*r*)] was determined using the indirect Fourier Transformation method in the SansView Program developed by the University of Tennessee as part of the Distributed Data Analysis of Neutron Scattering Experiments (DANSE) project.

Conflict of Interest: The authors declare no competing financial interest.

Acknowledgment. The authors would like to thank the ESPRC, AWE, and the University of Warwick for funding. The authors acknowledge Purac for the generous donation of lactide. T.H.E. and E.G.K. thank the NIH-NCRR COBRE grant, P20RR017716, for financial support. The statements herein do not reflect the views of NIH. E.G.K. also acknowledges support from a Department of Defense, Air Force Office of Scientific Research, National Defense Science and Engineering Graduate (NDSEG) Fellowship, 32 CFR 168a. We acknowledge the support of the National Institute of Standards and Technology, U.S. Department of Commerce, for providing the neutron research facilities used in this work. This work also benefitted from software developed by the DANSE project under NSF award DMR-0520547. We thank Dr. Jon Seppala for assistance with neutron scattering data collection and analysis. The SECs used in this research were obtained through Birmingham Science City, with support from Advantage West Midlands. We gratefully acknowledge financial support from EPSRC for the purchase of the Bruker Ultraflex MALDI-TOF MS instrument. The authors thank Dr. Ana Sanchez for HAADF-STEM imaging and valuable discussion, and they also acknowledge Dr. Ronan McHale, Dr. Nicole Hondow, Dr. Mike Ward, and Prof. Rik Brydson for assistance with the electron microscopy facilities at the Institute for Materials Research (SPEME), University of Leeds (funded by EPSRC). We thank the Science & Technology Facilities Council for the allocation of beam time, travel, and consumables grants at ISIS, and we thank Dr. Sarah Rogers for assistance with neutron scattering data collection and analysis.

Supporting Information Available: Detailed polymer synthesis and characterization, light scattering data, and additional microscopy images. This material is available free of charge *via* the Internet at http://pubs.acs.org.

REFERENCES AND NOTES

1. Moughton, A. O.; O'Reilly, R. K. Noncovalently Connected Micelles, Nanoparticles, and Metal-Functionalized Nanocages Using Supramolecular Self-Assembly. *J. Am. Chem. Soc.* **2008**, *130*, 8714–8725.
2. Dergunov, S. A.; Kesterson, K.; Li, W.; Wang, Z.; Pinkhassik, E. Synthesis, Characterization, and Long-Term Stability of Hollow Polymer Nanocapsules with Nanometer-Thin Walls. *Macromolecules* **2010**, *43*, 7785–7792.
3. Bolton, J.; Bailey, T. S.; Rzayev, J. Large Pore Size Nanoporous Materials from the Self-Assembly of Asymmetric Bottlebrush Block Copolymers. *Nano Lett.* **2011**, *11*, 998–1001.
4. Wakasugi, A.; Asakawa, M.; Kogiso, M.; Shimizu, T.; Sato, M.; Maitani, Y. Organic Nanotubes for Drug Loading and Cellular Delivery. *Int. J. Pharm.* **2011**, *413*, 271–278.
5. Kameta, N.; Masuda, M.; Minamikawa, H.; Mishima, Y.; Yamashita, I.; Shimizu, T. Functionalizable Organic Nanochannels Based on Lipid Nanotubes: Encapsulation and Nanofluidic Behavior of Biomacromolecules. *Chem. Mater.* **2007**, *19*, 3553–3560.
6. Donath, E.; Sukhorukov, G. B.; Caruso, F.; Davis, S. A.; Möhwald, H. Novel Hollow Polymer Shells by Colloid-Templated Assembly of Polyelectrolytes. *Angew. Chem., Int. Ed.* **1998**, *37*, 2201–2205.
7. Marinakos, S. M.; Novak, J. P.; Brousseau, L. C.; House, A. B.; Edeki, E. M.; Feldhaus, J. C.; Feldheim, D. L. Gold Particles as Templates for the Synthesis of Hollow Polymer Capsules. Control of Capsule Dimensions and Guest Encapsulation. *J. Am. Chem. Soc.* **1999**, *121*, 8518–8522.
8. Huang, H.; Remsen, E. E.; Kowalewski, T.; Wooley, K. L. Nanocages Derived from Shell Cross-Linked Micelle Templates. *J. Am. Chem. Soc.* **1999**, *121*, 3805–3806.
9. Raez, J.; Tomba, J. P.; Manners, I.; Winnik, M. A. A Reversible Tube-to-Rod Transition in a Block Copolymer Micelle. *J. Am. Chem. Soc.* **2003**, *125*, 9546–9547.
10. Kelley, E. G.; Smart, T. P.; Jackson, A. J.; Sullivan, M. O.; Epps, T. H., III Structural Changes in Block Copolymer Micelles Induced by Cosolvent Mixtures. *Soft Matter* **2011**, *7*, 7094–7102.
11. Zhang, L. F.; Eisenberg, A. Formation of Crew-Cut Aggregates of Various Morphologies from Amphiphilic Block Copolymers in Solution. *Polym. Adv. Technol.* **1998**, *9*, 677–699.
12. Wang, X.; Guerin, G.; Wang, H.; Wang, Y.; Manners, I.; Winnik, M. A. Cylindrical Block Copolymer Micelles and Co-Micelles of Controlled Length and Architecture. *Science* **2007**, *317*, 644–647.
13. Petzetakis, N.; Dove, A. P.; O'Reilly, R. K. Cylindrical Micelles from the Living Crystallization-Driven Self-Assembly of Poly(lactide)-Containing Block Copolymers. *Chem. Sci.* **2011**, *2*, 955–960.
14. Discher, D. E.; Eisenberg, A. Polymer Vesicles. *Science* **2002**, *297*, 967–973.
15. Zhang, L.; Eisenberg, A. Multiple Morphologies of "Crew-Cut" Aggregates of Polystyrene-b-poly(acrylic acid) Block Copolymers. *Science* **1995**, *268*, 1728–1731.
16. Zhang, Q.; Remsen, E. E.; Wooley, K. L. Shell Cross-Linked Nanoparticles Containing Hydrolytically Degradable, Crystalline Core Domains. *J. Am. Chem. Soc.* **2000**, *122*, 3642–3651.
17. Turner, J. L.; Wooley, K. L. Nanoscale Cage-like Structures Derived from Polyisoprene-Containing Shell Cross-linked Nanoparticle Templates. *Nano Lett.* **2004**, *4*, 683–688.
18. Samarajeewa, S.; Shrestha, R.; Li, Y.; Wooley, K. L. Degradability of Poly(Lactic Acid)-Containing Nanoparticles: Enzymatic Access through a Cross-Linked Shell Barrier. *J. Am. Chem. Soc.* **2012**, *134*, 1235–1242.
19. Stewart, S.; Liu, G. Block Copolymer Nanotubes. *Angew. Chem., Int. Ed.* **2000**, *39*, 340–344.
20. Stewart, S.; Liu, G. Hollow Nanospheres from Polyisoprene-block-poly(2-cinnamoylethyl methacrylate)-block-poly(tert-butyl acrylate). *Chem. Mater.* **1999**, *11*, 1048–1054.
21. Ho, R. M.; Chen, C. K.; Chiang, Y. W.; Ko, B. T.; Lin, C. C. Tubular Nanostructures from Degradable Core−Shell Cylinder Microstructures in Chiral Diblock Copolymers. *Adv. Mater.* **2006**, *18*, 2355–2358.
22. Boontongkong, Y.; Cohen, R. E. Cavitated Block Copolymer Micellar Thin Films: Lateral Arrays of Open Nanoreactors. *Macromolecules* **2002**, *35*, 3647–3652.
23. Sawyer, L. C.; Grubb, D. T. *Polymer Microscopy*, 2nd ed.; Chapman & Hall: London, UK, 1996.
24. Drummy, L. F.; Yang, J.; Martin, D. C. Low-Voltage Electron Microscopy of Polymer and Organic Molecular Thin Films. *Ultramicroscopy* **2004**, *99*, 247–256.
25. Allen, F. I.; Watanabe, M.; Lee, Z.; Balsara, N. P.; Minor, A. M. Chemical Mapping of a Block Copolymer Electrolyte by Low-Loss EFTEM Spectrum-Imaging and Principal Component Analysis. *Ultramicroscopy* **2011**, *111*, 239–244.
26. Gomez, E. D.; Panday, A.; Feng, E. H.; Chen, V.; Stone, G. M.; Minor, A. M.; Kisielowski, C.; Downing, K. H.; Borodin, O.; Smith, G. D.; et al. Effect of Ion Distribution on Conductivity of Block Copolymer Electrolytes. *Nano Lett.* **2009**, *9*, 1212–1216.
27. Zhao, H.; Chen, Q.; Hong, L.; Zhao, L.; Wang, J.; Wu, C. What Morphologies Do We Want? – TEM Images from Dilute Diblock Copolymer Solutions. *Macromol. Chem. Phys.* **2011**, *212*, 663–672.
28. Wang, Y.; Coombs, N.; Manners, I.; Winnik, M. A. Contrast Inversion in TEM Studies of Poly(ferrocenylsilane)-block-poly(dimethylsiloxane) Diblock Copolymers. *Macromol. Chem. Phys.* **2008**, *209*, 1432–1436.
29. Talmon, Y. Staining and Drying-Induced Artifacts in Electron Microscopy of Surfactant Dispersions. *J. Colloid Interface Sci.* **1983**, *93*, 366–382.
30. Wilson, N. R.; Pandey, P. A.; Beanland, R.; Young, R. J.; Kinloch, I. A.; Gong, L.; Liu, Z.; Suenaga, K.; Rourke, J. P.; York, S. J.; et al. Graphene Oxide: Structural Analysis and Application as a Highly Transparent Support for Electron Microscopy. *ACS Nano* **2009**, *3*, 2547–2556.

31. Patterson, J. P.; Sanchez, A. M.; Petzetakis, N.; Smart, T. P.; Epps, T. H., III; Portman, I.; Wilson, N. R.; O'Reilly, R. K. A Simple Approach to Characterizing Block Copolymer Assemblies: Graphene Oxide Supports for High Contrast Multi-Technique Imaging. *Soft Matter* **2012**, *8*, 3322–3328.
32. Petzetakis, N.; Walker, D.; Dove, A. P.; O'Reilly, R. K. Crystallization-Driven Sphere-to-Rod Transition of Poly(lactide)-b-poly(acrylic acid) Diblock Copolymers: Mechanism and Kinetics. *Soft Matter* **2012**, *8*, 7408–7414.
33. Moore, P. B. Small-Angle Scattering. Information Content and Error Analysis. *J. Appl. Crystallogr.* **1980**, *13*, 168–175.
34. Svergun, D. I.; Koch, M. H. J. Small-Angle Scattering Studies of Biological Macromolecules in Solution. *Rep. Prog. Phys.* **2003**, *66*, 1735–1782.
35. Glatter, O. Evaluation of Small-Angle Scattering Data from Lamellar and Cylindrical Particles by the Indirect Transformation Method. *J. Appl. Crystallogr.* **1980**, *13*, 577–584.
36. The average length of the cylindrical micelles prepared for the SANS experiments was 180 nm, as determined by TEM analysis (not shown). Input lengths ranging from 140 to 180 nm gave similar results for the radial cross-section determined from the P(*r*).
37. Kline, S. Reduction and Analysis of SANS and USANS Data Using IGOR Pro. *J. Appl. Crystallogr.* **2006**, *39*, 895–900.
38. Vagberg, L. J. M.; Cogan, K. A.; Gast, A. P. Light-Scattering Study of Starlike Polymeric Micelles. *Macromolecules* **1991**, *24*, 1670–1677.
39. Moffitt, M.; Yu, Y.; Nguyen, D.; Graziano, V.; Schneider, D. K.; Eisenberg, A. Coronal Structure of Star-Like Block Ionomer Micelles: An Investigation by Small-Angle Neutron Scattering. *Macromolecules* **1998**, *31*, 2190–2197.
40. Gilroy, J. B.; Gädt, T.; Whittell, G. R.; Chabanne, L.; Mitchels, J. M.; Richardson, R. M.; Winnik, M. A.; Manners, I. Monodisperse Cylindrical Micelles by Crystallization-Driven Living Self-Assembly. *Nat. Chem.* **2010**, *2*, 566–570.
41. Friedrich, H.; Frederik, P. M.; de With, G.; Sommerdijk, N. A. J. M. Imaging of Self-Assembled Structures: Interpretation of TEM and Cryo-TEM Images. *Angew. Chem., Int. Ed.* **2010**, *49*, 7850–7858.
42. Riley, T.; Heald, C. R.; Stolnik, S.; Garnett, M. C.; Illum, L.; Davis, S. S.; King, S. M.; Heenan, R. K.; Purkiss, S. C.; Barlow, R. J.; et al. Core−Shell Structure of PLA−PEG Nanoparticles Used for Drug Delivery. *Langmuir* **2003**, *19*, 8428–8435.
43. Riley, T.; Stolnik, S.; Garnett, M. C.; Illum, L.; Davis, S. S.; Taylor, P.; Tadros, T. F. Use of Viscoelastic Measurements for Investigating Interparticle Interactions in Dispersions of Micellar-like Poly(lactic acid)−Poly(ethylene glycol) Nanoparticles. *Langmuir* **2002**, *18*, 7663–7668.
44. Wilson, N. R.; Pandey, P. A.; Beanland, R.; Rourke, J. P.; Lupo, U.; Rowlands, G.; Römer, R. A. On the Structure and Topography of Free-Standing Chemically Modified Graphene. *New J. Phys.* **2010**, *12*, 125010.
45. Heenan, R. K.; Penfold, J.; King, S. M. SANS at Pulsed Neutron Sources: Present and Future Prospects. *J. Appl. Crystallogr.* **1997**, *30*, 1140–1147.